Overview of coordinated spherical tokamak research in Japan

メタデータ	言語: English
	出版者:
	公開日: 2023-03-29
	キーワード (Ja):
	キーワード (En):
	作成者: TAKASE, Yuichi, EJIRI, Akira, FUJITA, Takaaki, HANADA, Kazuaki, IDEI, Hiroshi, NAGATA, Masayoshi, ONCHI, Takumi, ONO, Yasushi, TANAKA, Hitoshi, TSUJII, Naoto, UCHIDA, M., YASUDA, K., KASAHARA, Hiroshi, MURAKAMI, Sadayoshi, TAKEIRI, Yasuhiko, TODO, Yasushi, TSUJI-IIO, Shunji, KAMADA, Yutaka
	メールアドレス:
	所属:
URL	http://hdl.handle.net/10655/00013584

Overview of coordinated spherical tokamak research in Japan

Y Takase[1], **A Ejiri**[1], **T Fujita**[2], **K Hanada**[3], **H Idei**[3], **M Nagata**[4], **T Onchi**[3], **Y Ono**[1], **H Tanaka**[5], **N Tsujii**[1], **M Uchida**[5], **K Yasuda**[2], **H Kasahara**[6], **S Murakami**[7], **Y Takeiri**[6], **Y Todo**[6], **S Tsuji-Iio**[8], **Y Kamada**[9]

[1] The University of Tokyo, Kashiwa 277-8561 Japan
[2] Nagoya University, Nagoya 464-8603 Japan
[3] Kyushu University, Kasuga 816-8580 Japan
[4] University of Hyogo, Himeji 671-2201 Japan
[5] Kyoto University, Kyoto 606-8502 Japan
[6] National Institute for Fusion Science, Toki 509-5292 Japan
[7] Kyoto University, Kyoto 603-8540 Japan
[8] Tokyo Institute of Technology, Tokyo 152-8550 Japan
[9] Naka Fusion Institute, QST, Naka 311-0193 Japan

E-mail: `takase@k.u-tokyo.acjp`

May 2021

Abstract. ST research in Japan has produced many innovative results: (i) Plasma start-up to $I_{\mathrm{p}} > 70\,\mathrm{kA}$ was achieved by ECW with $N_{\parallel} = 0.75$, whereas electron heating to $T_{\mathrm{e}} > 500\,\mathrm{eV}$ was achieved with $N_{\parallel} = 0.26$ on QUEST. (ii) RF-induced transport model combined with X-ray emission model, and extended MHD equilibrium with kinetic electrons were developed to interpret fast electron dominated LHW sustained plasmas on TST-2. (iii) Density as high as 30 times the cutoff density was achieved by EBW current drive combined with electron beam injection on LATE. (iv) Multiple plasmoids formed by tearing instability in the elongated current sheet were observed, and flux closure and ion heating by plasmoid-mediated fast magnetic reconnection were observed on HIST. (v) Optimization of ECW-assisted inductive start-up with vertical field with positive decay index was performed on TST-2. (vi) Stabilization of the vertical displacement event by a set of upper and lower helical field coils was demonstrated on TOKASTAR-2. (vii) 6-hour discharge was achieved by cool down of the center stack cover on QUEST, where plasma duration limit was consistent with the wall saturation time estimated by modelling. (viii) Extension of ion heating by plasma merging was achieved on TS-3U, TS-4U, UTST, MAST, and ST40.

Keywords: spherical tokamak, ST, plasma start-up, steady-state, high beta, reconnection, RF current drive, coaxial helicity injection

Submitted to: *Nucl. Fusion*

1. Introduction

Spherical tokamak (ST) research in Japan [1] is being conducted as a nationally coordinated program of university-scale ST devices under the ST Research Coordination Subcommittee organized by National Institute for Fusion Science (NIFS). Subcommittee members are leaders of ST research groups in Japan. The Subcommittee meets twice a year to discuss the overall strategy of Japanese ST research, exchange information on latest results, facilitate collaborations among different research groups, and coordinate participations in international collaborations. The roles of university ST research include: (1) unique research through creativity and innovation which might be considered too challenging for large ST devices, (2) establishment of the scientific basis for achieving ultra-high beta and ultra-long pulse (Fig. 1), (3) contribution to the scientific basis for practical and economically competitive fusion power, complementing the mainline tokamak research (JT-60SA, ITER, etc.), and (4) development and training of a future generation of world-leading tokamak scientists. Specific research topics include: (a) development of start-up, current drive, and control techniques without the use of the central solenoid (CS), (b) formation and sustainment of very high beta plasmas, and (c) demonstration of steady-state operation and the study of steady-state issues such as heat and particle control, divertor physics, and plasma-wall interaction.

In order to realize a compact fusion reactor with low aspect ratio, it is critically important to either eliminate the CS or minimize its size. There have been significant advances in the non-inductively driven current using radio-frequency (RF) waves in the electron cyclotron and lower hybrid frequency ranges, and in the understanding of physical processes involving high-energy electrons accelerated by RF waves. These are discussed in Sec. 2. Alternative methods using non-RF methods are discussed in Sec. 3. Very high density was achieved by combining the electron Bernstein wave and electron beam injection, the process of closed flux formation during plasma current start-up by transient coaxial helicity injection involving plasmoid-mediated fast magnetic reconnection was clarified, and an expansion of the pressure window (towards lower pressure) for inductive start-up using the trapped particle configuration with a weak vertical field with positive decay index was obtained with the help of EC wave preionization. In Sec. 4, stabilization of the vertical displacement event by superposition of a helical field was demonstrated using simple modular coils. A 6-hour long discharge was achieved by controlling recycling by wall temperature and the plasma duration limit was shown to be consistent with the wall saturation time, as discussed in Sec. 5. In Sec. 6, extension of the ion heating scaling by plasma merging (proportional to the square of the reconnecting magnetic field) up to $T_{\mathrm{i}} = 2.3\,\mathrm{keV}$ is reported. Finally, conclusions are given in Sec. 7.

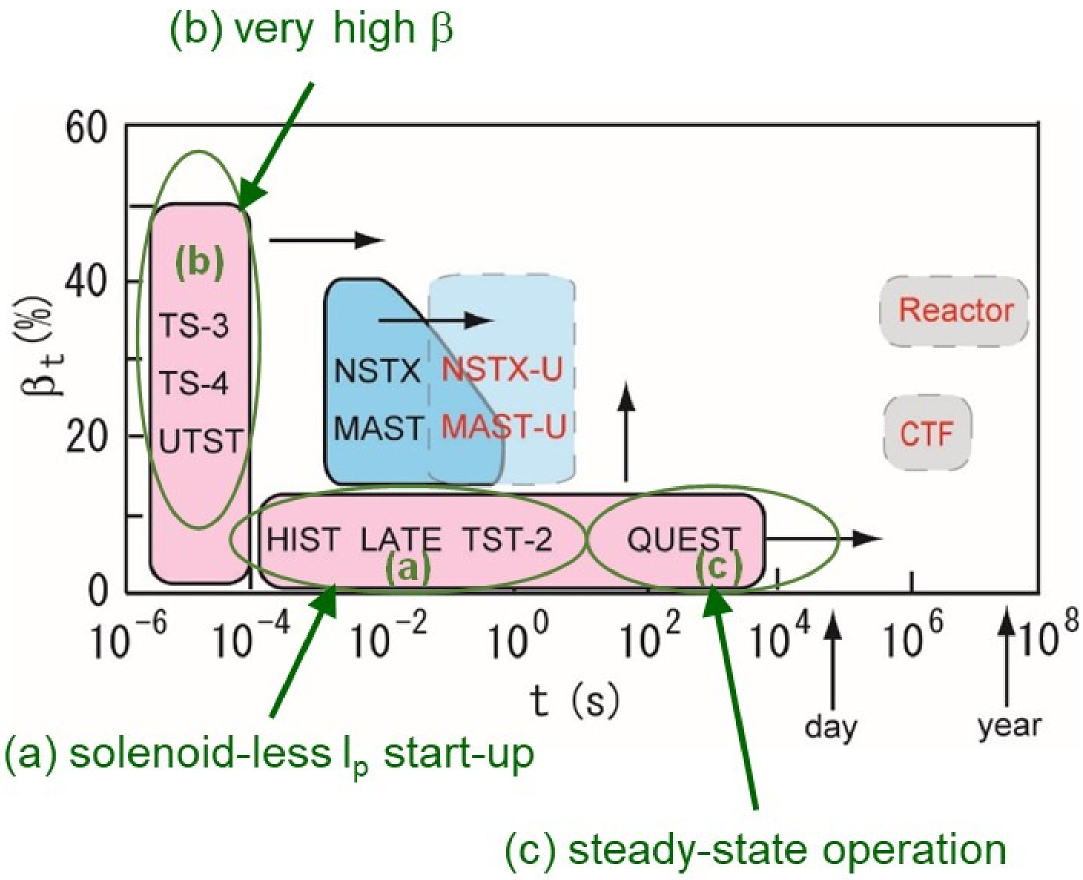

Figure 1. Japanese ST research strategy [1].

2. Plasma current start-up by RF waves

2.1. Electron cyclotron wave and electron Bernstein wave

Electron cyclotron wave (ECW) at 2.45 GHz and 5 GHz are used to excite the electron Bernstein wave (EBW) via O-X-B mode conversion on LATE (Kyoto U.). Highly overdense ST plasmas (up to 7 times the plasma cutoff density) are formed when the fundamental EC resonance layer is located in the plasma core, and EBW is excited in the 1st frequency band ($\omega_{\rm ce} < \omega < 2\omega_{ce}$) [2]. Whereas EBW in the 1st frequency band heats the bulk electrons, EBW in the 2nd frequency band ($2\omega_{\rm ce} < \omega < 3\omega_{ce}$) is absorbed by high-energy electrons and drives the plasma current ($I_{\rm p}$) [3]. $I_{\rm p}$ of up to 20 kA has been driven by EBW on LATE. Typical values of the current drive figure of merit $\eta_{\rm CD} = \overline{n}_{\rm e} I_{\rm p} R_0 / P_{\rm RF}$ is 2×10^{16} A/Wm^2.

Intermittent plasma ejections across the plasma boundary, synchronized with poloidal field decrement, were observed in highly overdense plasmas. In the short duration ($\sim 100\,\mu$sec) of the ejection phenomenon, oscillations in the Alfven frequency range appear and an increase of the space potential in the plasma from ~ 20 eV to

$\sim 70\,\mathrm{eV}$ was observed, suggesting the loss of high-energy electrons [4].

Electron cyclotron heating (ECH) assists plasma breakdown and reduces the loop voltage V_l for I_p start-up in conventional tokamaks [5], [6]. The ECH and current drive (CD) have key roles in the scenario of non-inductive start-up for spherical tokamaks [7]–[10]. In QUEST, I_p is ramped up primarily by the 28 GHz ECW with multiple harmonic resonance layers, from the second to the fourth, in the plasma core [11]. Owing to the steering antenna consisting of two quasi-optical mirrors installed recently, the power density of the ECW around the harmonic resonance layers is enhanced [12]. In addition, the incident angle of the RF beam can be adjusted. Since the second harmonic resonance layer located at $R_\mathrm{res2} = 0.32\,\mathrm{m}$ is close to the inboard limiter at $R = 0.23\,\mathrm{m}$, the parallel refractive index $N_\parallel$ can be high. I_p ramp-up experiments were conducted over the range $0.1 < N_\parallel < 0.9$ at R_res2. According to the resonance condition, energetic electrons moving in the forward direction (to increase I_p) resonate more effectively than those moving in the backward direction. Such asymmetry is consistent with the results of the I_p ramp-up experiment, in which I_p exceeds 70 kA by injecting a constant RF power of 100 kW [11]. η_CD of up to $6\times10^{17}\,\mathrm{A/Wm^2}$ has been achieved using 28 GHz on QUEST, compared to typical values of $5\times10^{16}\,\mathrm{A/Wm^2}$ using 8.2 GHz.

As shown in Fig. 2, the addition of a moderately low V_l ($< 0.5\,\mathrm{V}$) increases I_p up to 100 kA. Hard X-rays (HXR) emitted by forward electrons are shown in Fig. 2(e). The flux surfaces are shown in Fig. 2(f), and the ray trajectories calculated for the experimental condition with $N_\parallel = 0.75$ at R_res2 are shown in Fig. 2(g). The polarization of the injected wave was dominantly X-mode in this experiment.

A quasi-normal injection of ECW was also conducted. Compared to oblique injection, the number of energetic electrons is lower. In the experiment with $N_\parallel = 0.26$ at R_res2, bulk electrons are heated effectively, and the electron temperature reaches $T_\mathrm{e} > 500\,\mathrm{eV}$ even though plasma I_p is less than 30 kA. The waveforms are presented in Fig. 3. The area of closed magnetic surfaces is much smaller than the oblique injection case, as shown in Fig. 3(e). According to TASK/WR, RF power is absorbed by bulk electrons around the second harmonic resonance layer. Assuming $T_\mathrm{e} = 500\,\mathrm{eV}$ at the resonance, 7% of the RF power is absorbed by bulk electrons in a single pass. This result demonstrates that the control of $N_\parallel$ is an important element for I_p ramp-up in STs.

2.2. Lower-hybrid wave

The lower hybrid wave (LHW) is known to be an efficient current driver in conventional tokamaks. Experiments using LHW were performed on TST-2, and I_p of up to 27 kA was generated [13], but the current drive efficiency is low (η_CD of typically of order $10^{17}\,\mathrm{A/Wm^2}$) and needs to be improved. In order to interpret the behaviours of energetic electrons, an RF-induced transport model combined with an X-ray emission model is proposed. Fig. 4 shows a schematic configuration of the electron transport model. A cold electron starting from a magnetic surface is accelerated along the magnetic field

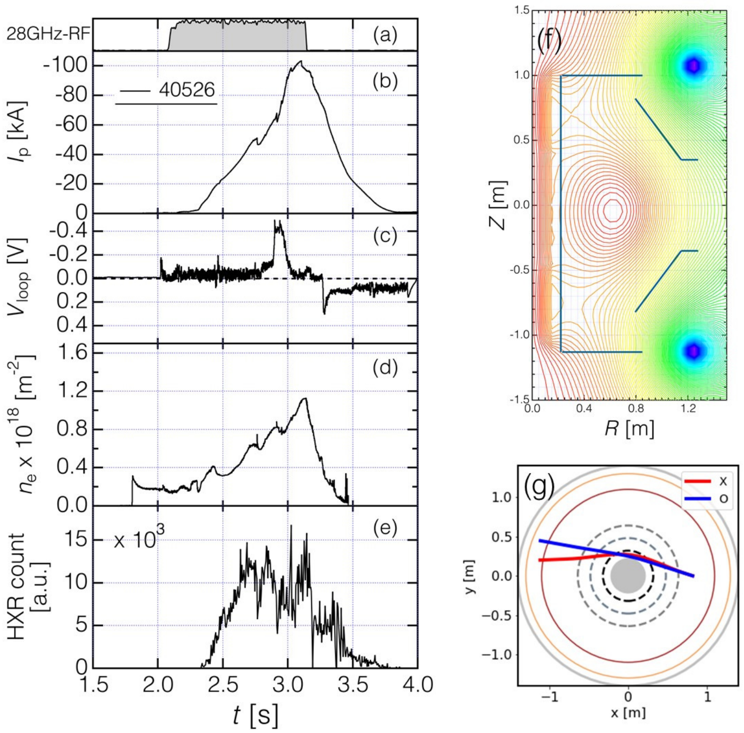

Figure 2. (a) 28 GHz power, (b) I_{p}, (c) V_{l} at the central post, (d) line-integrated density, (e) forward HXR count rate, (f) flux surfaces at $I_{\mathrm{p}} = 100\,\mathrm{kA}$, and (g) rays calculated by TASK/WR.

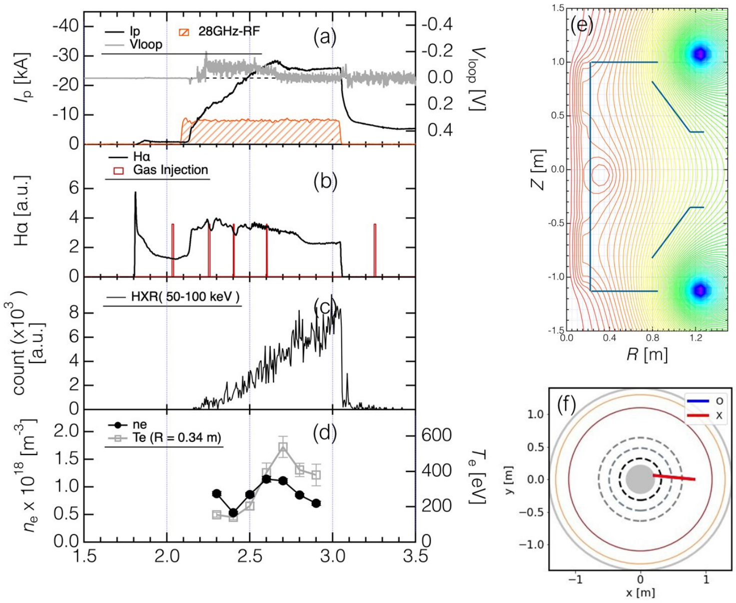

Figure 3. (a) 28 GHz power, Ip, and Vl, (b) H_{α} emission and gas injection pulses, (c) forward HXR count rate, (d) electron density and temperature measured by Thomson scattering, (f) flux surfaces at $I_{\mathrm{p}} = 30\,\mathrm{kA}$, and (g) rays calculated by TASK/WR.

line by the LHW electric field. With the increase in the parallel velocity the orbit deviates from the magnetic surface, and the electron would hit the outboard limiter or the inboard limiter. Besides the LHW electric field, collisions with ions, electrons and neutrals would decelerate the electron, by which the orbit moves inward. The effect of the LHW electric field is simulated by a random walk in velocity space, which also induces a spatial random walk. The electron reaching the limiter is lost, and a new cold electron is supplied by an electron impact ionization of a neutral molecule. The new electron is placed on a given magnetic surface. The neutral density should be adjusted to keep the steady state. By following many electrons we would obtain a velocity distribution function. From the analysis of the obtained state, the power from LHW to fast electrons, collisional heating power of cold electrons, the current carried by fast electrons, and the particle confinement time can be calculated. The details of the model are described in Ref. [14]. After a sufficient calculation time, we obtain a steady state electron velocity distribution function and energy distribution of lost electrons. The latter is used to calculate the thick target X-ray emission. The model includes several free parameters, and some of them are adjusted to reproduce the experimental plasma current, the LHW injected power, the electron density, and some of them are set to be the same as the measured values.

An X-ray emission model is constructed to predict the measured HXR spectrum for the steady-state fast electrons. Details of the model are described in [14]. Figure 5 shows the HXR spectra from two similar discharges with almost the same plasma current of $I_\mathrm{p} = 18\,\mathrm{kA}$ and the LHW power of $P_\mathrm{RF} \simeq 60\,\mathrm{kW}$. The major difference between them is the outboard LCFS position $R_\mathrm{LCFS} = 0.515\,\mathrm{m}$ and $0.54\,\mathrm{m}$ (see Fig. 4 for the definition of R_LCFS). The difference in R_LCFS would cause a difference in R_sout. Thus, we set the outboard starting point $R_\mathrm{sout} = 0.495\,\mathrm{m}$ and ,$0.520\,\mathrm{m}$ for the two cases. Here R_souts were chosen so that $R_\mathrm{LCFS} - R_\mathrm{sout}$ are the same for the two discharges. Most of other parameters are the same for the two cases. The spectral shapes of the two discharges and the ratio of fluxes are well reproduced by the simulation, but the measured and the calculated absolute fluxes are different by a factor of 9 (Fig. 5). In addition to the HXR spectra we can calculate the power flow and the particle confinement time. Of the injected LHW power of 60 kW, about 10 kW heats the bulk electrons, and additional 10 kW heats ions and neutrals. The residual power of 40 kW is lost by fast electrons hitting the limiters. Using the bulk electron heating power and an appropriate energy confinement time, we can estimate the bulk electron temperature, which is consistent with the experimental measurement . This electron transport model can reproduce the major features of the fast electrons in LHW sustained TST-2 plasmas.

In low-density start-up plasmas driven solely by LHW, I_p is believed to be carried mostly by the LHW driven fast electrons. Since the electrons are accelerated predominantly in the direction parallel to the magnetic field by electron Landau damping, the fast electron velocity distribution function may become highly anisotropic. In addition, due to the low I_p during the start-up phase, the electron orbit excursions from the flux surfaces may be substantial. As a result, fast electrons may carry current in

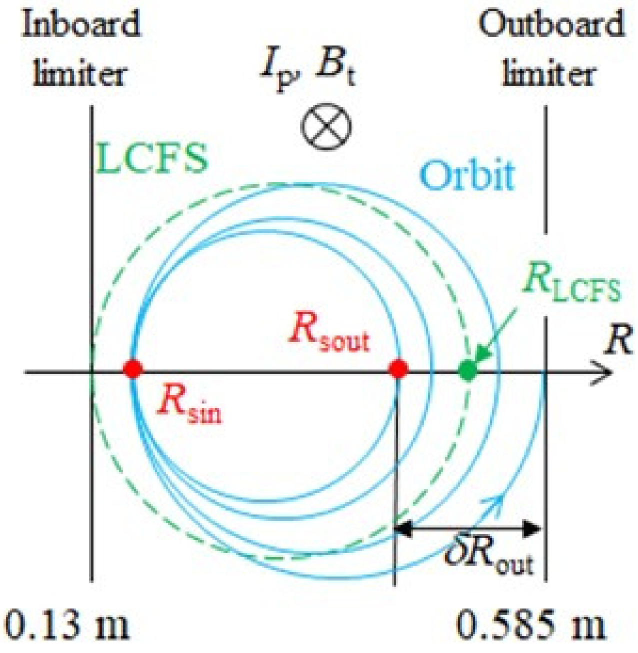

Figure 4. Schematic configuration in a poloidal plane. The solid curve shows the orbit of an electron accelerated 3 times at the position $R_{\rm sin}$. The corresponding outboard starting position is $R_{\rm sout}$, and the distance between $R_{\rm sout}$ and the outboard limiter (at $R = 0.585\,\rm m$) is defined as $dR_{\rm out}$. The outboard last closed flux surface (LCFS) position is $R_{\rm LCFS}$.

the scrape-off-layer (SOL) which cannot be described trivially with the standard Grad-Shafranov equation. The impact of collisionless fast particles on MHD can be studied by considering an extended MHD model with a two-component plasma of bulk MHD fluid and kinetic fast particles [15], [16]. Since the magnetic field is generated by fast particles as well as the bulk fluid, the fast particle dynamics couple to the bulk equations through the fast particle current. Recently, a new equilibrium reconstruction code was developed to analyze non-inductive $I_{\rm p}$ start-up plasmas driven by LHW on TST-2 [17]. The collisionless fast electrons were treated kinetically and the orbit-averaged distribution function was written in terms of the total energy, the magnetic moment, the parallel velocity sign and the toroidal angular momentum. The distribution function was parameterized in terms of the perpendicular temperature, parallel plateau energy limits, and the inner and outer radius limits of the fast electrons. The plateau energy limits and the outer radius limit could be estimated from the standard wave and Fokker-Planck analysis [18]. By setting the perpendicular temperature to the bulk electron temperature that can be measured, and fixing the total fast electron current, only the inner radius limit remains as a free parameter. This parameter was optimized as well as the parameters of the two free functions (the bulk pressure and poloidal current) to

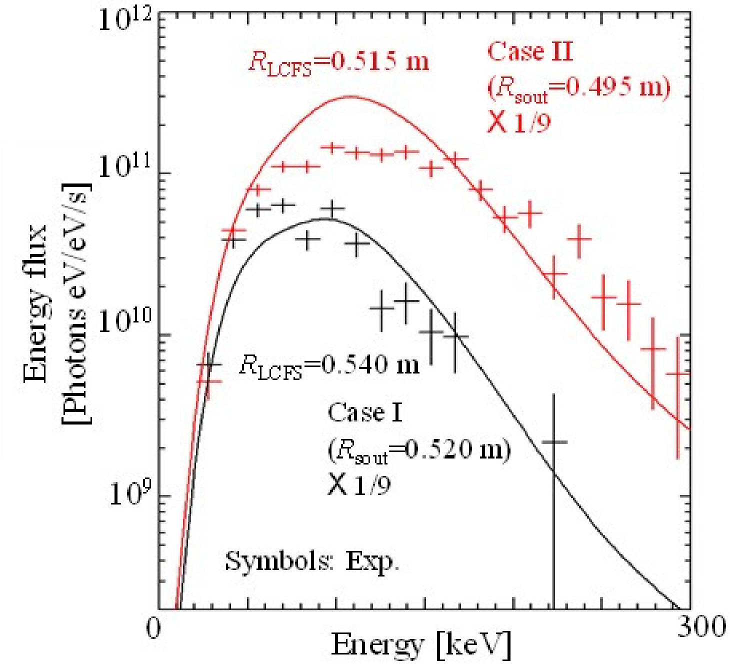

Figure 5. Simulated (solid curve) and measured (plus symbols) energy spectra are compared. The simulated spectra are multiplied by a factor of 1/9 in the plot.

reconstruct an equilibrium that was a solution to the extended MHD equations.

The result of the extended MHD analysis performed on a typical top-launch LHW driven plasma on TST-2 is shown in Fig. 6. The toroidal current profile reconstructed with fast electrons (b) was more concentrated on the high-field side compared to that without fast electrons (a). The reconstructed current profile with fast electrons reflected the strong $1/R$ dependence, because the parallel current density is approximately proportional to the magnetic field strength. Although this dependence is similar to the bulk poloidal current function, the fast electron current could extend into the low-field side SOL which had an effect of reducing the bulk pressure function substantially. The change in the current profile resulted in a more peaked poloidal flux function. The fitting error of the (bulk) electron density profile decreased when the flux function with extended MHD was used, which means that the reconstructed poloidal flux function was more consistent with the measurement assuming that the electron density profile was a flux function. This may indicate that the fast electrons indeed modify MHD equilibrium in a way that cannot be described by the standard GS equation. Note the modification discovered here originates from the strong $1/R$ dependence of the magnetic field strength of a spherical tokamak, and may be weak for conventional high-aspect ratio tokamaks.

Both results obtained from the RF-induced transport model and the extended MHD equilibrium indicate the strong influence of the $1/R$ dependence of $B_{\rm t}$. The field line length and the residence time of the fast electrons become large on the inboard side, leading to the inboard RF power deposition and a higher current density on the inboard

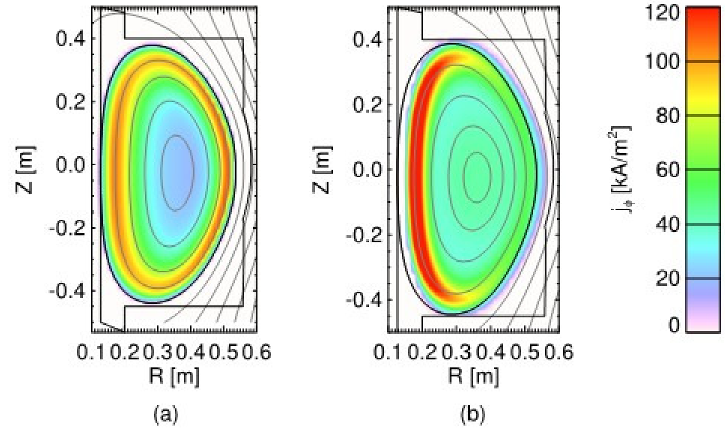

Figure 6. The reconstructed toroidal current density without fast electrons (a) and with 70% of the plasma current carried by fast electrons (b).

side. In addition, the fast electron density and the current density in the outboard side scrape-off layer become large. The extended MHD model can represent equilibrium without any closed flux surfaces, so it can be used to seamlessly describe the early phase of RF start-up when the closed flux surfaces are not formed. Such a framework will allow us to better control and optimize start-up scenarios where collisionless fast electrons play a dominant role. According to the results of the RF-induced transport model, a few times higher density and outboard power deposition are preferable for increasing the driven current. With an appropriate density increment, collisions would reduce the gradual orbit loss, but the density increment should be moderate not to eliminate the fast electrons themselves. Outboard power deposition would move the orbit towards the magnetic axis, and the gradual orbit loss can be avoided. Obviously, wave physics must be considered to realize such a change. A new approach or a new antenna design considering these new effects is necessary for further increase of the driven current.

3. Plasma current start-up by non-RF methods

3.1. Electron beam injection

For further increase of the electron density, temperature and plasma current during the start-up phase, electron beam injection (EBI) is attempted on LATE. Expected effects are direct and effective injection of momentum to drive the current and energy to heat electrons and ions. In addition, combined with EBW, electron beam with energy of several keV may be created resonantly by Dopper-shifted EBW and drive current efficiently. An attempt of EBI into an overdense ST plasma produced non-inductively by EBW and investigation of synergistic effects of EBI and EBW has begun [19].

An electron beam injector with Mo cathode head is installed on the bottom side ($R_\mathrm{c} = 0.255\,\mathrm{m}$, $Zc = -0.45\,\mathrm{m}$) of the LATE device. The emission surface is set normal to the toroidal direction. When a plasma contacts the Mo cathode head and a negative voltage relative to the vacuum vessel is applied to the head, the plasma works as an anode and an electron beam is extracted and flows into the plasma roughly along the magnetic field lines. The direction of the beam is the same as that of the toroidal field B_{t} and drift of electrons which carry the plasma current I_{p}. The collision of the beam with the injector and/or the bottom wall after one turn around the torus may be avoided because of the large pitch of the magnetic field ($B_{\mathrm{v}}/B_{\mathrm{t}} \simeq 1/13$). The power supply for EBI consists of a capacitor bank (20 kV, 250 μF) and two ignitron switches, one for start and the other for commutation to stop. Resistors (10 Ω in total) are connected in series to regulate the cathode current. Hydrogen gas is fed through slits in the cathode head to mitigate the ion bombardment.

Figure 7 shows a typical discharge where a negative cathode voltage of $V_{\mathrm{k}} = -10\,\mathrm{kV}$ is applied at time $t = 0.17\,\mathrm{s}$ in an ST plasma produced by 26 kW of 2.45 GHz microwave power. The microwave is injected through open circular waveguide type antennas set obliquely to B_{t} at the angle of 72 degrees at $R = 0.5\,\mathrm{m}$. A half of the injected microwave power is linearly polarized with the electric field perpendicular to B_{t} (X-mode like) and the other half is left-handed circularly polarized (O-mode like). B_{t} is 0.072 T and the electron cyclotron resonance (ECR) layer is located at $R = 0.206\,\mathrm{m}$. When V_{k} is applied, I_{p} decreases by 0.5 kA in about 0.1 ms, then begins to increase as the cathode current I_{k} starts. However, V_{k} is reduced quickly because of low cathode impedance compared with the resistors and significant increment of I_{p} is not observed. I_{p} saturates as the electron density n_{e} increases rapidly, while I_{k} is about 800 A. I_{p} may be driven by EBW and EBI, but its large increment may be inhibited because the vertical filed B_{v} is constant at 0.053 T after $t = 0.16\,\mathrm{s}$ without feedback control. Before $t = 0.1703\,\mathrm{s}$ when I_{p} saturates, faster increase of soft X-ray emission I_{sx} from the plasma center compared to that of n_{e} is observed, suggesting the possibility of a strong electron heating, but a more direct evidence is needed. As shown in Fig. 8(a), the bright region of the fast CCD camera image coincides well with the LCFS obtained by magnetic reconstruction, although the right side is mostly blocked by the reflection mirror for the 7 GHz interferometer. In addition, there is a very bright emission in the lower right region near the center post ($R < 0.1\,\mathrm{m}$). The cathode head is not visible in the camera image, but is located at the bottom of the vacuum vessel, 60° away toroidally from the CCD camera port. This bright region is believed to be caused by EBI because the ECR layer is located at $R = 0.206\,\mathrm{m}$, but the precise mechanism is not well understood at present. The electron density n_{e} increases with a maximum value of $1.7 \times 10^{18}\,\mathrm{m}^{-3}$ near the ECR layer [Fig.8(b)]. These results suggest effective heating by EBW and/or EBI. At $t = 0.1705\,\mathrm{s}$, n_{e} becomes saturated and I_{p} begins to decrease. At this time, n_{e} reaches $2.3 \times 10^{18}\,\mathrm{m}^{-3}$ which is more than 30 times the plasma cutoff density. I_{sx} and n_{e} are maintained during EBW and EBI until EBI is turned off at $t = 0.171\,\mathrm{s}$. However, the calculated mode-conversion rate for left-handed circularly polarized wave reduces from 70% to 40% and I_{p}, I_{sx} and n_{e} decrease rapidly after EBI turns off. LCFS disappears at $t = 0.1715\,\mathrm{s}$ and finally I_{p} terminates at $t = 0.1763\,\mathrm{s}$.

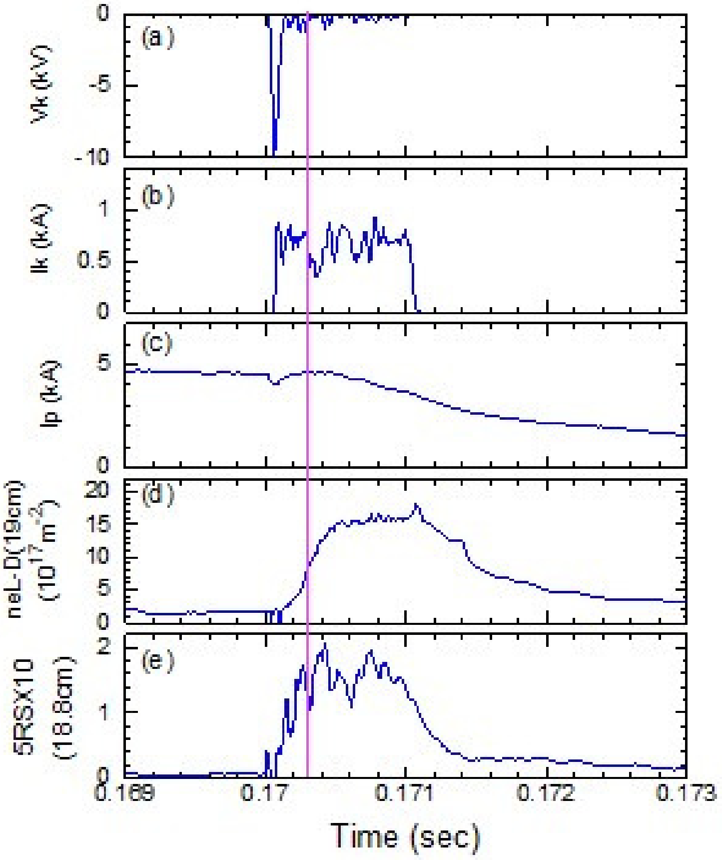

Figure 7. (a) Cathode voltage V_k, (b) cathode current I_k, (c) plasma current I_p, (d) line-integrated electron density at the tangency radius of $R_\mathrm{T} = 0.19\,\mathrm{m}$, (e) soft X-ray emission at $R_\mathrm{T} = 0.188\,\mathrm{m}$. 2.45 GHz microwave power of 26 kW is injected till $t = 0.180\,\mathrm{s}$. The red line shows the time $t = 0.1703\,\mathrm{s}$ referred to in Fig. 8.

In this first experiment, the cathode impedance is very low and the energy of injected electrons is several hundred eV, which is effective to ionize neutrals to increase the density but not effective to drive current. The production of metallic impurities caused by ion bombardment at the cathode head should be considered. For effective combined heating and current drive by EBW and EBI, it is necessary to develop a new cathode whose impedance is large enough to inject electrons with energy more than several keV and the electron density should be controlled to a mild level such as $1.7 \times 10^{18}\,\mathrm{m}^{-3}$ in this experimental condition.

3.2. Transient coaxial helicity injection

The key role of plasmoid-mediated magnetic reconnection has been experimentally investigated during transient-coaxial helicity injection (T-CHI) for non-inductive plasma start-up on HIST. The fast magnetic reconnection is required for the flux closure in T-CHI discharges. Here, we have found that, (i) during the helicity injection phase, a

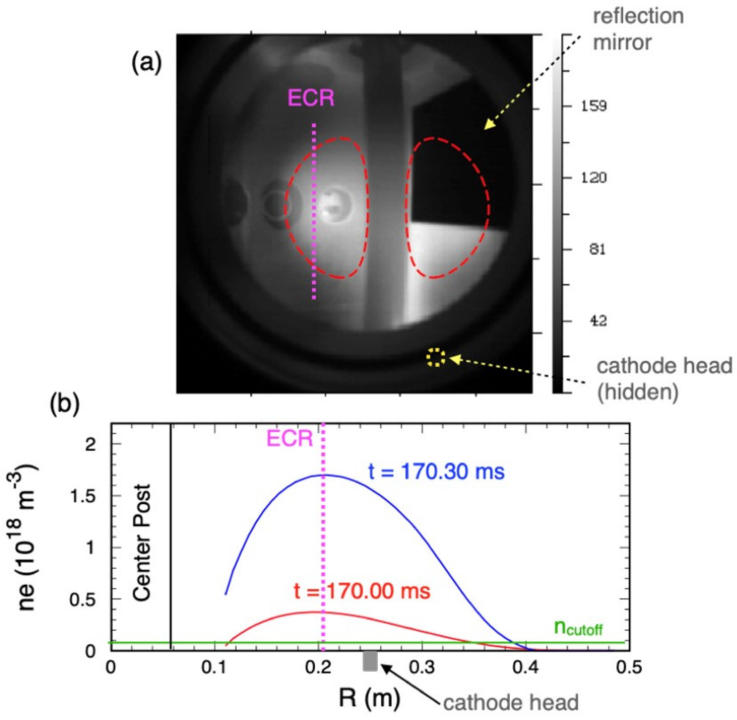

Figure 8. (a) CCD camera image taken at $t = 0.1703\,\mathrm{s}$ with shutter time of $10\,\mu\mathrm{s}$. The red dashed line shows the LCFS obtained by magnetic reconstruction. The position of the ECR layer is shown by the magenta dotted line at $R = 0.206\,\mathrm{m}$. The cathode head is located 60° away toroidally from the CCD camera port. (b) Electron density radial profile by Abel inversion from a 4 ch 70 GHz interferometer signals.

current sheet is elongated and broken apart at some points inside it due to a tearing instability, so that a small-size plasmoid is newly born in sequence by being divided due to reconnection from a bigger plasmoid. The separation and coalescence of the multiple plasmoids are repeated through reconnection. (ii) Doppler ion temperature increased from 10–20 eV up to 80 eV during T-CHI. The ion heating driven by the plasmoid reconnection was identified on HIST for the first time. (iii) The plasmoid evolves to a large-scale closed flux surface due to inward current diffusion during the resistive decay phase [20].

For fusion reactors, non-inductive current drive methods, such as various helicity injection techniques and subsequent RF or NB injection are required for steady-state operation. T-CHI non-inductive plasma start-up method [21] could realize compact reactor designs based on ST without the central solenoid coil. This method needs the magnetic reconnection at the X point for generating a high quality closed flux during the plasma injection phase. The magnetic reconnection is well known to heat ions effectively by converting from magnetic energy to kinetic energy. The application of reconnection heating can be expected for the T-CHI. At present, one of the most important issues for T-CHI is whether it can establish enough closed flux surfaces and plasma heating by driving the magnetic reconnection as fast as possible.

According to a recent MHD numerical simulation on T-CHI [22], the reconnection rate based on the plasmoid instability is much faster than that by Sweet-Parker (S-P) model even in the high Lundquist number S regime. Understanding the mechanism of fast plasmoid reconnection for flux closure and related ion heating is the primary objective of the T-CHI experiment on HIST device [23]. Figure 9 shows the time evolutions of the toroidal plasma current, the electron density, the poloidal flux at $Z = 0.37\,\mathrm{m}$, the reconnection electric field calculated by $E_\mathrm{t} = -(d\Psi_\mathrm{p}/dt)/(2\pi R)$ at the X-point at $R = 0.25\,\mathrm{m}$, $Z = 0.318\,\mathrm{m}$. The plasma is injected from the coaxial magnetized plasma gun (MCPG) into the flux conserver (FC) and decays due to plasma resistivity. The regular oscillations with the frequency of $175\,\mathrm{kHz}$ can be seen in n_e, Ψ_p, and E_t between $t = 170\,\mu\mathrm{s}$ and $220\,\mu\mathrm{s}$. The ion Doppler temperature increases to 30–40 eV between $t = 150\,\mu\mathrm{s}$ and $170\,\mu\mathrm{s}$, proceeding up to 80 eV. These oscillations indicate that small-size plasmoids are repeatedly generated in the elongated current sheet by reconnection. Fig. 10 shows the 2D contour plots of Ψ_p and toroidal current density J_t (a), and of E_t (b), calculated from the data obtained by internal magnetic field measurements. J_t and E_t are in the θ direction of the R-θ-Z cylindrical coordinate system. It is noted that the current sheet is elongated by the pull $\boldsymbol{J} \times \boldsymbol{B}$ force from the MCPG and there are three small-size plasmoids inside it. Results from the E_t contours exhibit that its polarity changes at the reconnection points during one cycle of the plasmoid oscillation in the elongated current sheet.

In summary, the experimental investigation has revealed the process of plasmoid-driven magnetic reconnection during T-CHI on HIST. The experimental findings are: (1) the separation and coalescence processes of plasmoids are repeated after the elongated current-sheet becomes unstable during CHI current start-up; (2) ion heating is enhanced due to the repetitive reconnection during the plasmoid oscillation.

3.3. Optimization of inductive plasma current ramp-up

Ohmic start-up of tokamaks with superconducting central solenoid can be challenging due to the low V_l. Pure Ohmic breakdown requires a high quality field-null region to last for a sufficiently long time, which becomes increasingly difficult at low V_l. On the other hand, breakdown is easily obtained by injecting ECW. ECW has been applied to Ohmic start-up, in the field-null configuration (FNC), to assist breakdown. ECW has also been used successfully for non-inductive tokamak start-up. In the non-inductive start-up scenario, a vertical field with positive decay index, i.e., the trapped particle configuration (TPC), is required. The curved vertical field is required to confine the collisionless fast electrons which can be trapped in the magnetic well in the absence of closed flux surfaces. Such a field structure allows closed flux surfaces to form spontaneously with sufficient ECW power. In addition, it has also been known that this vertical field configuration is required to obtain reliable ECW breakdown in the high ECW power and/or low-pressure regime.

Recently, it was found that the TPC was beneficial not only for non-inductive I_p

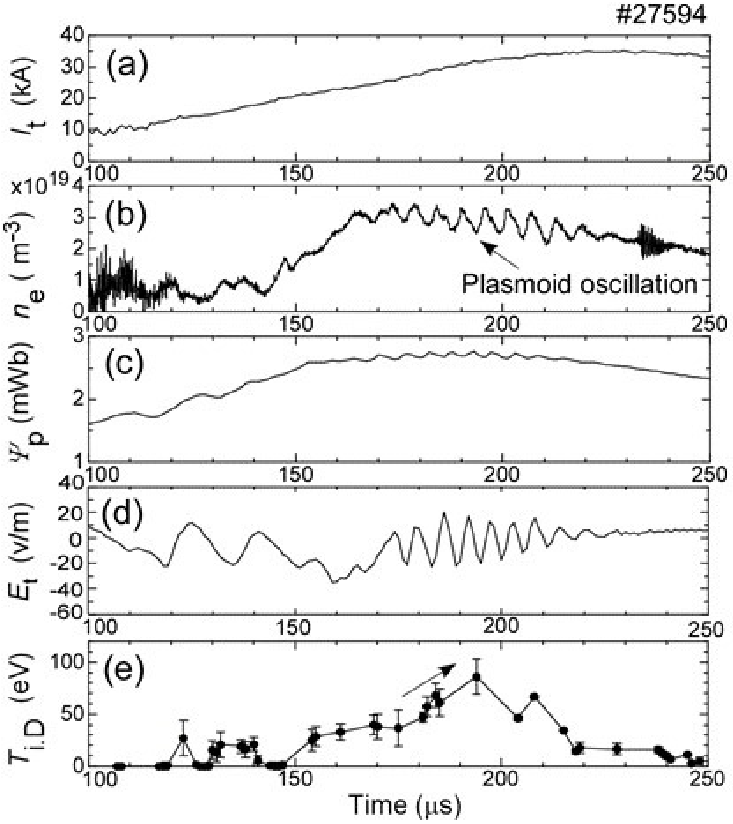

Figure 9. Time evolution of the toroidal current I_{t} (a), the electron density n_{e} (b), the poloidal flux Ψ_{p} (c), the reconnection electric field E_{t} (d), and Doppler ion temperature $T_{\mathrm{i.D}}$ (e).

start-up, but also for ECW assisted inductive I_{p} start-up [24], [25]. The effect of the poloidal field configuration on ECW assisted Ohmic start-up was studied further in TST-2, with focus on the difference between the TPC and the FNC in the high ECW power and low-pressure regime [26]. To newly develop a TPC start-up scenario, a curved vertical field of 4 mT was superimposed on top of the standard FNC start-up waveform. Since the poloidal field was $< 1\,\mathrm{mT}$ for the FNC start-up, this created the desired vertical field structure (TPC) in the presence of Ohmic coil swing. The prefill pressure was scanned at the same ECW power and V_{l} waveform to see the effect of the poloidal field configuration on I_{p} start-up. The result is shown in Fig. 11. The inductive electric field was 0.3 V/m at the EC resonance ($R = 0.32\,\mathrm{m}$) where breakdown was assumed to start (the loop voltage was 0.6 V). The EC frequency was 2.45 GHz and the EC power was 5 kW. It can be seen that the low-pressure limit, determined by successful initiation of breakdown, was lower (pressure window is expanded) for the TPC start-up compared to the FNC start-up. Although we were not able to demonstrate operation at lower loop voltage due to the coil power supply constraint, we believe that expansion of the operational neutral pressure window to the low-pressure side with the TPC will allow for startup at a lower loop voltage. The I_{p} ramp-up rate was also greater for the TPC start-

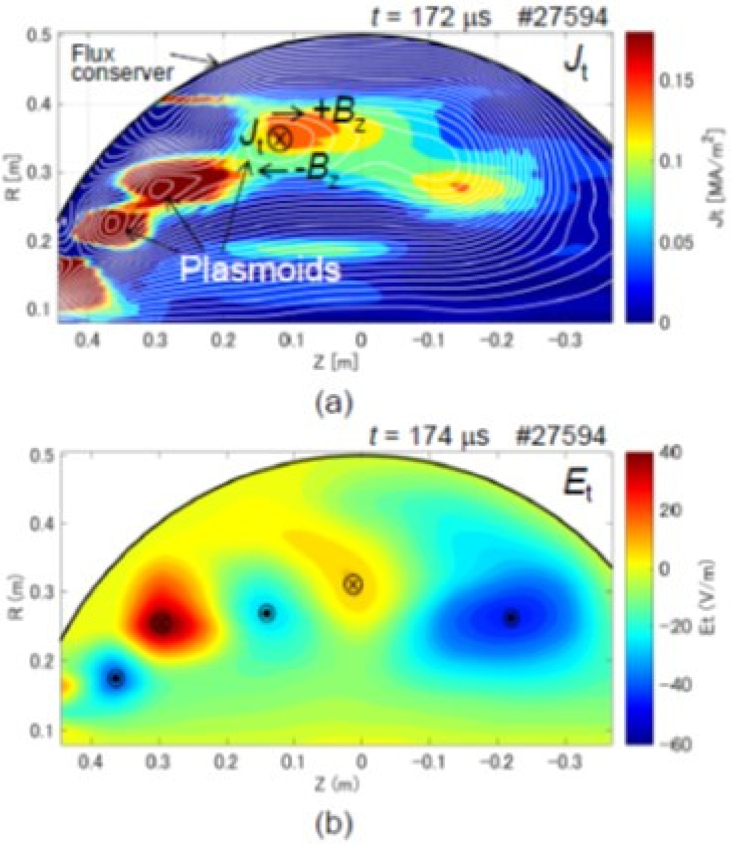

Figure 10. 2D contour plots of the poloidal flux Ψ_p and the toroidal current density J_t (a), and of the toroidal electric field E_t (b) on the R-Z poloidal plane in the FC.

up especially at low prefill pressure. These observations can be understood in terms of the difference in confinement mechanism between the two configurations. In the FNC, electrons are confined due to collisions with neutral gas which decreases when accelerated by EC waves to higher velocity. In contrast, TPC is designed to maximize confinement of collisionless fast electrons. Therefore, TPC's better confinement of fast electrons may have resulted in faster breakdown and broader operational window to lower pressure. On the other hand, the high-pressure limit, determined by successful burn-through, was nearly the same for the TPC and the FNC. This indicates that at high pressure, collisionless electrons, and hence, the poloidal field structure and the electron orbits, do not play a dominant role. ECW assistance affects I_p start-up simply in terms of the global power balance between Ohmic/ECW heating and radiation/ionization losses.

4. Stabilization of tokamak plasma using helical field coils

TOKASTAR-2 is a tokamak-stellarator hybrid device with a small aspect ratio ($\simeq 2.5$). It is equipped with parallelogram-shaped partial helical field coils and is capable of forming closed flux surfaces without the plasma current. The main objectives of this

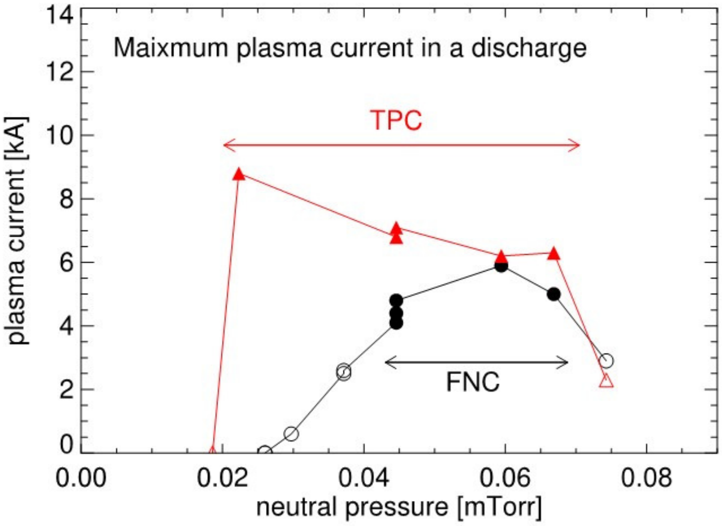

Figure 11. The low pressure limit for successful I_{p} start-up is extended to the lower pressure region in TPC compared to FNC.

device are to evaluate the effects of helical field application on tokamak plasma and to study the effects of the plasma current on compact stellarator configuration. One of the effects expected in helical field application on tokamak plasma is stabilization of plasma position. The effective axisymmetric poloidal field component of the helical field pushes the plasma column toward the magnetic axis of the helical field, if its rotational transform has the same sign as that by the poloidal field generated by the plasma current. The effect was shown for both the horizontal and vertical directions in [27], and for the vertical direction in [28]. One of the concerns on the use of helical field is the complexity of adding helical field coils to tokamak coils. Continuously-wound helical coils were used in [28] and semi-stellarator coils such that each coil covers upper, outboard and lower sides were used in [27]. Compared to those coils, the local helical coils of TOKASTAR-2 are simpler because they are separately located on upper, outboard and lower sides. The local helical coils of TOKASTAR-2 consists of two parallelogram-shape coils, called HF coils, located on the outboard side, and four fan-shape coils, called AHF coils, located on the upper and lower sides. The effect of the helical field application on the plasma horizontal position was observed with magnetic field measurements [29], [30] and with a high-speed camera [31], [32] in TOKASTAR-2. Suppression of vertical instability was also studied in elongated plasmas but no clear effects of the helical field were observed [33]. It was found that the effective radial field B_r^{eff} generated by helical coils was not appropriate for stabilizing the plasma vertical movement. The B_r^{eff} is evaluated by

$$B_r^{\mathrm{eff}} = \int_{\phi=0}^{2\pi} B_r ds \Bigg/ \int_{\phi=0}^{2\pi} ds$$

where B_r is the radial component of the magnetic field, ϕ is the toroidal angle, and ds is the infinitesimal arc length along a field line. Rotational transform generated by the helical field was used to evaluate the stabilizing effects of the helical field in a previous study [30]. Note that B_r^{eff} can be evaluated even when no closed flux surfaces are generated by helical field while the rotational transform can be evaluated only when closed flux surfaces are generated.

New local helical coils were designed and manufactured so that a large stabilizing B_r^{eff} could be obtained [33]. The new coils, named ULT coils, are shown in Fig. 12(a), which are triangular-shape coils located on the upper and lower sides. The number is two on the upper side and two on the lower side. The discharges with and without the helical field generated by the ULT coils are shown in Fig. 12(b). In both discharges, the vertical field and the horizontal field were applied to adjust the horizontal and vertical plasma positions respectively, while the quadrupole field was applied to increase the plasma elongation. No feed-back control of the plasma position and shape was made. The current of the horizontal field coil was kept constant while the current of the vertical field coil and that of the quadrupole field coil varied during the plasma discharge according to the discharge of capacitor banks. The details of the poloidal field coils and the waveforms of the coil currents are described in Ref. [33]. In the case without the ULT field, the elongation started to increase gradually at $t \simeq 2.65\,\mathrm{ms}$, and finally the upward vertical displacement event (VDE) and the plasma current quench occurred.

In the case with the ULT field, the horizontal position was farther inside, where the decay index of the vertical field was more negative than in the discharge without the ULT field. Even with more negative decay index, the VDE was suppressed by applying the ULT field as shown by red curves. The ULT coil current was 4.8 kAturns. The radial and vertical positions of the plasma current centroid (R_J and Z_J) and the plasma elongation were evaluated by the filament method using field measurements along the poloidal limiter [30]. Figure 12(c) shows the visible light intensity distribution measured with a high-speed camera. These images also show clearly that the upward VDE occurred in the discharge without the ULT field while the VDE was suppressed in the discharge with it. The light intensity of the plasma with the ULT magnetic field was weaker than that without the ULT magnetic field. One possible cause is lower electron density and/or lower electron temperature in the plasma with the ULT field, but the density and temperature measurements are not available yet. The direction of plasma vertical movement during VDE depended on the plasma vertical position Z_J before VDE occurrence. Through systematic scan in Z_J with the horizontal field for several values of the ULT coil current and the current of the coil for elongating the plasma, it was observed that the range in Z_J where VDE did not occur became wider with the ULT coil current and narrower with the current of the coil for elongating the plasma. This clearly indicates that the ULT coil current has a stabilizing effect for VDEs. Although suppression of vertical instability by coils on the upper and lower sides only was predicted theoretically [34], [35], this is the first experiment that demonstrated it. This implies that the outboard-side coils can be eliminated in addition to the inboard-side coils for vertical stabilization, which makes the coil system simpler and improves its feasibility. The non-axisymmetric fields applied for the improvement of vertical stability might have

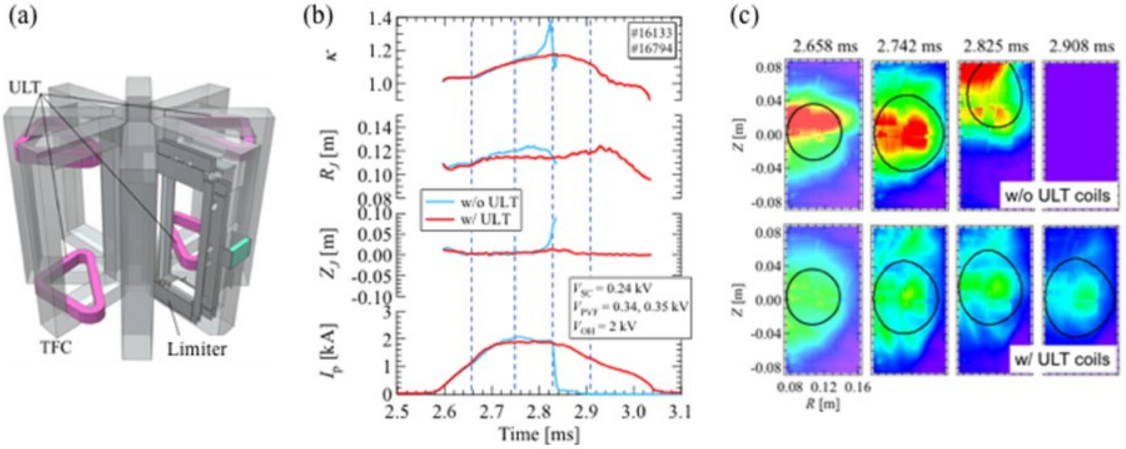

Figure 12. Suppression of vertical position instability with local top and bottom coils in TOKASTAR-2. (a) Schematic view of the local top and bottom coils, ULT coils, in pink, limiter and toroidal field coils (TFCs). (b) Waveforms of discharges with and without using ULT coils, shown by red and blue curves respectively. From the top, the plasma elongation, the major radius of the current centroid, the vertical height of the current centroid and the plasma current are shown. (c) Visible camera images of the same discharges shown in (b). The light intensity is converted to colors. Black lines in images denote the last closed flux surfaces estimated by the magnetic measurements..

an influence on tokamak plasma confinement. The influence is suggested by camera images shown in Fig. 12(c). This problem needs to be studied both experimentally and theoretically in the future.

5. Demonstration of steady-state operation by wall temperature control

Steady state operation (SSO) is a crucial issue for a fusion power plant. QUEST has been addressing this issue using a hot wall with the capability to control the temperature of plasma facing walls (PFWs) [36], [37]. The effective pumping capability of external pumps was about $6\,\mathrm{m}^3/\mathrm{s}$, and the time-averaged number of evacuated H atoms was about 1×10^{17} H/s in long duration discharges on QUEST. This corresponds to 10% of the wall pumping rate at the beginning of the discharge (1×10^{18} H/s). The achieved pulse duration is plotted as a function of wall temperature in Fig. 13. The result clearly indicates that the higher wall temperature results in shorter pulse duration. This tendency can be explained by wall saturation, where the desorbed H flux from the wall becomes equal to the wall injected H flux. The wall saturation time τ_{WS} is derived using a hydrogen barrier model based on microscopic observation of plasma-exposed specimen by nuclear reaction analysis (NRA) [37]. According to the model, τ_{WS} can be expressed as

$$\tau_{\mathrm{WS}} = \left(\frac{d_{\mathrm{dep}}^2}{\gamma_{\mathrm{W}} k_{\mathrm{rec}}}\right)^{1/2},$$

where d_{dep}, γ_{w}, and k_{rec} denote the thickness of the deposition layer, influx of hydrogen to a unit area of PFWs, and the recombination coefficient, respectively. The wall-area averaged value of d_{dep} is approximately 10–30 nm [38], depending on their location and plasma operation. Especially, the direction of the toroidal drift makes an up-down asymmetry of the deposition layer thickness. The value of γ_{w} can be estimated by the calibrated H_α signal level [37] and is about $1 \times 10^{17}\,\mathrm{H/m^2/s}$ for the longest discharges at each wall temperature. The value of k_{rec} for the specimens exposed to QUEST plasma was measured by NRA during plasma exposure [39], and is expressed by

$$k_{\mathrm{rec}} = 4 \times 10^{-36} \exp\left(-\frac{1972}{T[\mathrm{K}]}\right).$$

We select these values and over-plot the calculated time for wall saturation, where the out-flux of H is equal to the influx of H into the wall. They are far from the experimental values as shown in Fig. 13. The main reason is the effect of trapping and de-trapping in the plasma facing materials. The effect of trapping and de-trapping has been investigated and the effect was identified by thermal desorption spectrum (TDS) for a plasma-exposed specimen [40] and can be described by the equations

$$\begin{aligned}\frac{dH_{\mathrm{W}}(t)}{dt} &= S_{\mathrm{W}}\gamma_{\mathrm{W}} - \frac{k_{\mathrm{rec}}}{S_{\mathrm{W}} d_{\mathrm{dep}}^2} H_{\mathrm{W}}^2(t) - \frac{dH_{\mathrm{T}}(t)}{dt} \\ \frac{dH_{\mathrm{T}}(t)}{dt} &= \frac{D}{\lambda^2} H_{\mathrm{W}}(t)\left(1 - \frac{H_{\mathrm{T}}(t)}{H_{\mathrm{T0}}}\right) - \nu_0 \exp\left(-\frac{E_{\mathrm{D}}}{T}\right) H_{\mathrm{T}}(t).\end{aligned} \tag{1}$$

Here, H_{W}, H_{T}, and H_{T0} represent the number of solved, trapped hydrogen (H), and the maximum number of trapped H, respectively. And S_{W}, D, λ, ν_0 and E_{T} denote the surface area, diffusion coefficient, lattice constant of material, Debye frequency ($= 10^{13}\,\mathrm{s}^{-1}$), and activation energy for de-trapping, respectively. We use the following expressions,

$$\begin{aligned}&D = 3.8 \times 10^{-7} \exp\left(-\frac{0.41\,[\mathrm{eV}]}{T}\right)\ [\mathrm{m^2/s}] \\ &E_{\mathrm{T}} = 0.51\,[\mathrm{eV}] \\ &H_{\mathrm{T0}} = 3 \times 10^{21}\ [\mathrm{H/m^2}].\end{aligned} \tag{2}$$

It should be noted that the value of k_{rec} is 10 times larger than that in TDS measurement, because the wall during plasma experiment may be cleaner. And the area integrated maximum number of trapped H is assumed to be constant at 3×10^{21} [H] [40], [41]. The calculated duration required to reach wall saturation, where wall injected H flux is equal to desorbed H flux, agrees with plasma duration as shown in Fig. 13. This indicates that the plasma duration is limited by wall saturation based on the trapping and de-trapping effect of the deposition layer. Several significantly shorter durations are observed around 400 K and longer durations at 473 K. The shorter durations give rise to insufficient wall conditioning including a small air leak. As for the longer durations, the main difference comes from the replacement of the center stack cover from stainless steel coated by APS-W to 316L stainless steel panels. The

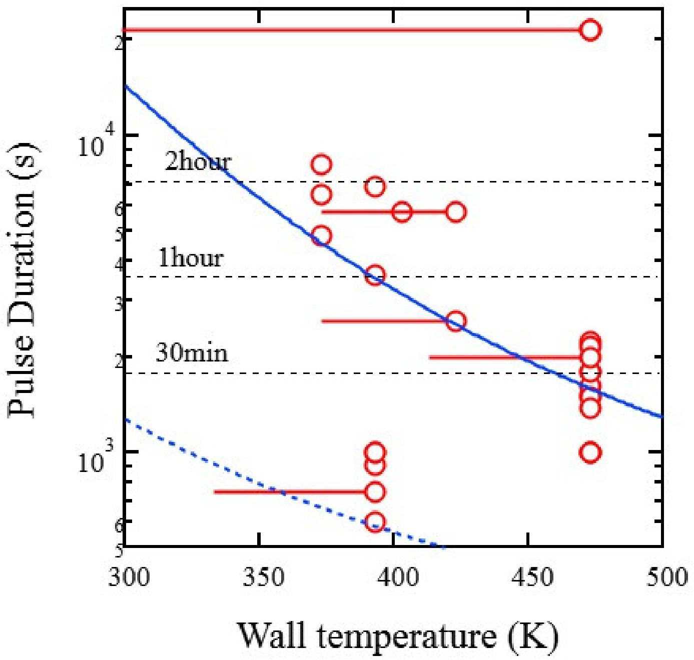

Figure 13. Achieved plasma durations with RF current drive are plotted as a function of wall temperature on QUEST. Horizontal error bar indicates the distribution of wall temperature including water cooling during the discharge. The RF power is in the range of 40–60 kW, and the electron density is about 2×10^{17} m−3. The solid and dotted lines represent the required time to reach wall saturation for the deposition layer with the trapping effect and τ_{WS}, respectively.

replacement was done in the summer of 2018. According to a previous study [41], the APS-W surface did not play a main role in particle balance, because the APS-W surface behaves like pure tungsten that just stores a small amount of H. On the other hand, the property of stainless steel for H is quite complicated, because of the presence of significant oxide layer and trapping sites (desorption peak $\simeq$ 400 K) as close as the operation temperature of the plasma devices. However, the wall pumping capability of the newly installed stainless steel plays a significant role in achieving longer durations.

Particle balance for one day, including a 6-hour discharge at the wall temperature of 473 K, is shown in Fig. 14. It should be noted that the wall temperature of the center stack cover ($\simeq$ 300 K) is significantly lower than that of the hot wall due to water cooling. The number of injected H_2 was 1.5 times larger than another 6h discharge at 473 K before the installation of the stainless steel panels on the center stack cover. The wall saturation took place around 10,000 s from the beginning of the plasma, because the injected H_2 was kept constant after that time. The surface area of the center stack cover ($\sim 3\,\mathrm{m}^2$) corresponds to only 12% of the total wall area, but the effect on particle balance was remarkable. According to Fig. 13, the predicted time for wall saturation is less than 2,000 s, but the observed duration for wall saturation was longer by over a factor of 5. This clearly indicates that the local wall temperature modification has a

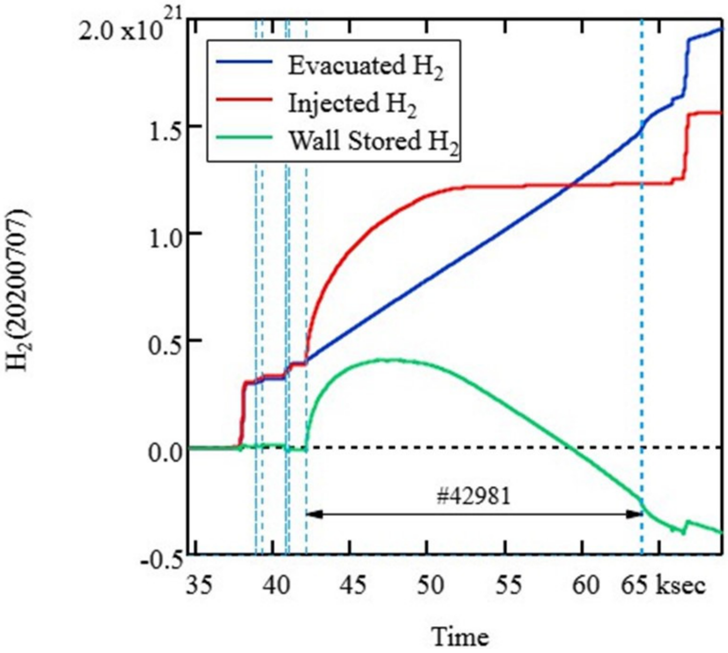

Figure 14. Particle balance for one day including a 6h discharge (# 42981). Red, blue, and green lines represent the number of injected, evacuated, and trapped H converted to the number of H_2. The dotted vertical lines indicate each shot timing. The start of the horizontal line is 0:00 on 7 July 2020.

potential to control the gross particle balance. This provides a candidate to avoid density runaway through local wall temperature regulation. When the wall is saturated, a part of wall temperature ramps down and the recovery of wall pumping may prevent density runaway. After this, the wall temperature should be increased gradually and may be allowed to return to the original temperature. If this wall temperature cycle is realized, we can achieve steady state particle balance. Moreover, this data clearly indicates an evidence of shot history. The wall stored H became negative and all the injected H_2 was evacuated halfway into the plasma and the H emission from the plasma facing wall is overbalance. This overbalance is supported by wall-stored H in previous experiments and is likely to induce unknown H emission. The unknown H emission frequently gives rise to density runaway. To identify and control this unknown H emission is one of the most important issues for achieving steady state operation. Although these experiments were performed at low density and low current, the density runaway caused by wall saturation, described in this manuscript, gives rise to radiation collapse, reduction of electron temperature and plasma current, and leads to a termination of the tokamak plasma, and is common to tokamaks at higher densities and higher currents.

6. Access to high temperature plasma regime

The high-power reconnection heating of merging ST plasmas has been developed by ST merging experiments TS-3(U), TS-4(U), UTST, MAST and ST40 and by PIC simulations [42]–[44]. All of these researches confirmed that the reconnection heating energy (mostly for ions) scales with the square of the reconnecting magnetic field B_{rec} which is approximately the poloidal magnetic field if the common flux between two STs is negligible. The ST merging experiment on ST40 achieved the maximum ion temperature of $T_{\mathrm{i}} \simeq 2.3\,\mathrm{keV}$ for the electron density of $n_{\mathrm{e}} \simeq 1.5 \times 10^{19}\,\mathrm{m}^{-3}$. This promising scaling suggests a new possibility of direct access to burning plasmas by reconnection heating, without the use of any additional heating such as neutral beam injection (NBI). It is noted that this scaling needs (1) compression of the current sheet (formed by the two merging ST plasmas) to the order of ion gyro-radius, and (2) low linked flux between ST plasmas and the walls or coils. The details of this research will be presented in another overview paper IAC/P4-3 for ST plasma merging experiments and simulations [45].

7. Conclusions

ST research in Japan has produced many innovative results since the last IAEA Fusion Energy Conference in 2018, as summarized below. (i) I_{p} start-up with ECW/EBW is being investigated on LATE and QUEST. On QUEST, I_{p} start-up to $> 70\,\mathrm{kA}$ was achieved by quasi-parallel injection with $N_{\parallel} = 0.75$, whereas electron heating to $T_{\mathrm{e}} > 500\,\mathrm{eV}$ was achieved by quasi-perpendicular injection with $N_{\parallel} = 0.26$. (ii) I_{p} start-up with LHW is being investigated on TST-2. RF-induced transport model combined with X-ray emission model reproduced the measured HXR spectra, and extended MHD equilibrium with kinetic electrons showed important modification due to fast electrons. (iii) e-beam injected to an EBW-driven ST plasma on LATE resulted in a density increase up to 30 times the cut-off density, and significant core heating was observed but not further I_{p} ramp-up. (iv) Multiple plasmoids are formed by tearing instability in the elongated current sheet, and flux closure and ion heating by plasmoid-mediated fast magnetic reconnection were observed on HIST. (v) Optimization of ECW-assisted inductive start-up with vertical field with positive decay index was performed on TST-2. Low pressure limit for I_{p} start-up was extended to lower pressure region in TPC, and I_{p} ramp-up was higher for TPC. (vi) Stabilization of VDE by a set of upper and lower triangular coils was demonstrated on TOKASTAR-2. (vii) 6-hour dischargees were achieved by cool down of the center stack cover on QUEST, where the plasma duration limit was consistent with the wall saturation time estimated by modelling. (viii) Ion heating by plasma merging, which scales as the square of the reconnecting magnetic field, was extended to MAST and ST40, and the ion temperature of 2.3 keV was achieved on ST40.

Acknowledgments

The Committee on Coordinated ST Research in Japan is supported by NIFS/NINS under the project of Promotion of International Network for Scientific Collaborations URSX306. The work on TST-2 was supported by the NIFS Collaboration Research Programs NIFS18KOAR022 and NIFS20KUTR155, and by the Japan/US Cooperation in Fusion Research and Development. The work on LATE was supported by JSPS Grant-in-Aid for Scientific Research (A) 18H03689 and (B) 18H01198. The work on QUEST was supported by Grant-in-Aid for JSPS Fellows 16H02441 and 19H05526, and by the NIFS Collaboration Research Programs NIFS05KUTRO14, NIFS13KUTRO93, NIFS13KUTRO85, and NIFS14KUTR103, and in part by the Collaborative Research Program of the Research Institute for Applied Mechanics, Kyushu University. The work on TOKASTAR-2 was supported by the NIFS Collaboration Research Program NIFS17KLEP026. The joint work of TS-3U, MAST and ST-40 was supported by JSPS Grant-in-Aid for Scientific Research (S) 15H05750 and (A) 20H00136.

References

[1] Takase Y *et al* 2017 *Nucl. Fusion* **57** 102005
[2] Tanaka H *et al* 2016 *Proc. 26th IAEA Fusion Energy Conference 2016* IAEA-CN-234/EX/P4-45
[3] Tanaka H *et al* 2018 *Proc. 27th IAEA Fusion Energy Conference 2018* IAEA-CN-258/EX/P3-19
[4] Tanaka H *et al* 2014 *Proc. 26th IAEA Fusion Energy Conference 2014* IAEA-CN-211/EX/P7-4
[5] Jackson G L *et al* 2009 *Nucl. Fusion* **49** 115027
[6] Stober J *et al* 2011 *Nucl. Fusion* **51** 083031
[7] Uchida M *et al* 2010 *Phys. Rev. Lett.* **104** 065001
[8] Maekawa T *et al* 2012 *Nucl. Fusion* **52** 083008
[9] Idei H *et al* 2017 *Nucl. Fusion* **57** 126045
[10] Idei H *et al* 2020 *Nucl. Fusion* **60** 016030
[11] Onchi T *et al* 2021 *Phys. Plasmas* **28** 022505
[12] Idei H *et al* 2019 *Fusion Eng. Des.* **146** 1149
[13] Yajima S *et al* 2018 *Plasma Fusion Res.* **13** 3402114
[14] Ejiri A *et al* 2021 *Proc. 28th IAEA Fusion Energy Conference 2020* IAEA-CN–286/EX/P7-17
[15] Todo Y and Bierwage A 2014 *Plasma Fusion Res.* **9** 3403068
[16] Belova E V, Gorelenkov N N and Cheng C Z 2003 *Phys. Plasmas* **10** 3240
[17] Tsujii N *et al* 2020 *Plasma Fusion Res.* **15** 2402010
[18] Tsujii N *et al* 2017 *Nucl. Fusion* **57** 126032
[19] Tanaka H *et al* 2021 *Proc. 28th IAEA Fusion Energy Conference 2020* IAEA-CN–286/EX/P7-18
[20] Nagata M et al 2016 Proc. 26th IAEA Fusion Energy Conference 2016 IAEA-CN-234/EX/P5-21
[21] Raman R *et al* 2010 *Phys. Rev. Lett.* **104** 095003
[22] Ebrahimi F *et al* 2019 *Phys. Plasmas* **26** 092502
[23] Nagata M *et al* 2018 *Proc. 27th IAEA Fusion Energy Conference 2018* IAEA-CN-258/EX/P3-17
[24] Ani Y *et al* 2016 *Nucl. Fusion* **57** 016001
[25] Lee J *et al* 2017 *Nucl. Fusion* **57** 126033
[26] Ko Y *et al* 2021 *Plasma Fusion Res.* **16** 1402056
[27] Ikezi H and Schwarzenegger K F 1979 *Phys. Fluids* **22** 2009
[28] Archmiller MC *et al* 2014 *Phys. Plasmas* **21** 056113
[29] Ueda T *et al* 2015 *Plasma Fusion Res.* **10** 3402065
[30] Yasuda K *et al* 2018 *Plasma Fusion Res.* **13** 3402072

[31] Sakito T *et al* 2016 *Plasma Fusion Res.* **11** 2402074
[32] Takase Y *et al* 2017 *Nucl. Fusion* **57** 102005.
[33] Yasuda K *et al* 2020 *Plasma Fusion Res.* **15** 1402083
[34] Reiman A *et al* 2007 *Phys. Rev. Lett.* **99** 135007
[35] Turnbull A D *et al* 2016 *Nucl. Fusion* **56** 086006
[36] Hanada K *et al* 2017 *Nucl. Fusion* **57** 126061
[37] Hanada K *et al* 2019 *Nucl. Fusion* **59** 076007
[38] Oya Y *et al* 2019 *Fusion Eng. Des.* **146** 1480–1484
[39] Murakami T *et al* 2017 *Proc. ICFRM-18 Aomori Japan 2017* 8PT37
[40] Hanada K *et al* 2015 *Journal of Nuclear Materials* **463** 1084–1086
[41] Hanada K *et al* 2021 *Nuclear Materials and Energy*, to be published
[42] Ono Y *et al* 2019 *Nucl. Fusion* **59** 076025
[43] Ono Y *et al* 2011 *Phys. Rev. Lett.* **107** 185001
[44] Gryaznevich M P *et al* 2019 *AIP Conference Proc. 2179* 020008
[45] Ono Y *et al* 2021 *Proc. 28th IAEA Fusion Energy Conference 2020* IAEA-CN-286/IAC/P4-3